Electron-hole interactions in silicon nanocrystals

Kevin Leung and K. B. Whaley
Department of Chemistry, University of California, Berkeley, California 94720
(Received 13 December 1996; revised manuscript received 8 May 1997)

We investigate the electron-hole interactions in spherical silicon nanocrystals by incorporating Coulomb, exchange, and spin-orbit couplings into a tight-binding model. We study the effect of the electron-hole attraction on the absorption spectra and on the dielectric constant, using a real-time propagation technique. Diagonalizing the full fine-structure Hamiltonian for two-particle states close to the band gap gives exchange splittings that range from ~100 to 7 meV for nanocrystals of radii 6–18 Å. The splittings persist in the presence of spin-orbit coupling for nanocrystals of radius up to 18 Å, suggesting that dark triplet states below the absorption threshold can be the origin of the Stokes shifts and temperature-dependent lifetimes observed in luminescence experiments. [S0163-1829(97)09635-5]

I. INTRODUCTION

It is well known that the band gap of nanoscale quantum dots are blueshifted from the bulk value due to quantum confinement.[1,2] Finite-size effects also enhance the band-edge oscillator strengths of indirect gap materials such as silicon.[1,2] The fine structures in the optical spectra of silicon nanocrystals and porous silicon are also different from those in the bulk. This is essentially due to size-dependent changes in the effect of the Coulomb interaction. In the strong-confinement regime, i.e., when the crystallite is smaller than the bulk exciton diameter, the electron and the ''hole'' are in close proximity, and the Coulomb interaction scales as $1/a$, where a is the linear dimension of the nanocrystal. The static dielectric constant ϵ_s also decreases with crystallite size,[3] further increasing the effect of the electron-hole attraction at small a. A strong Coulomb interaction perturbs the energy levels, mixes the zeroth-order eigenstates, and leads to a reassignment of oscillator strengths, which can have noticable effects in the absorption spectra $\sigma_{\mathrm{abs}}(\omega) \sim \omega \epsilon_2(\omega)$. ϵ_s is derived from $\epsilon_2(\omega)$, and is in turn therefore also affected by the strength of the electron-hole Coulomb attraction.[4] In fact the finite-size-induced change in dielectric screening can drive a nanocrystal of a particular size from the weak-confinement into the strong-confinement regime.[3]

The excitonic exchange splitting η is proportional to the overlap between electron and hole wave functions in silicon nanocrystals,[4] and scales as $1/a^3$. For small a, the bulk silicon exchange interaction of 0.14 meV (Ref. 5) can be increased by up to three orders of magnitude.[4,6] This interaction creates low-lying triplet states that do not absorb or emit light. Spin-orbit coupling then mixes the otherwise pure singlets and triplets. When the mixing is small, the triplets can be populated nonradiatively after optical excitation into the singlet manifold, and then luminesce with long lifetimes. This ''two-level'' model has been advanced as an explanation for the Stokes shifts and the temperature-dependent luminescence lifetimes found in porous silicon.[4,7–9] In this two-level picture, the Stokes shifts correspond to η. At temperatures $k_B T \geqslant \eta$, where k_B is the Boltzmann constant, the singlet, bright states are thermally accessible, and radiative decay readily takes place. The lifetime crossover occurs at $T > 100$ K, consistent with the experimental Stokes shifts of ~10 meV.[10] The model is therefore very sensitive to the relative magnitudes of the exchange and spin-orbit couplings. When η is small compared to the spin-orbit coupling, extensive singlet/triplet mixing may occur, and dark states may not exist on the strength of exchange interaction alone. However nonspherical crystallite shapes can quench the spin-orbit coupling and help preserve the singlet-triplet splittings, so that geometry may also play an important role.[11,12]

Coulomb and exchange effects in silicon nanocrystals have been investigated previously with the multiband effective mass approximation (EMA) (Ref. 4) and other continuum models.[6] EMA also successfully treats spin-orbit coupling in direct-gap nanocrystals such as CdSe.[13,14] However, silicon does not have purely s-conduction states at the band gap, which complicates the analysis.[4] In contrast, the two-particle extension of the tight-binding method is well suited to studying the combined effects of Coulomb, exchange, and spin-orbit interactions.[12] It gives a more realistic representation of small nanocrystals than quasicontinuum theories, and surface effects can be accounted for readily. In this paper, we apply the tight-binding description of a previous work[15–17] that uses an sp^3s^* basis.[18] The nanocrystals studied here are tetrahedrally faceted, i.e., approximately spherical in shape, with either truncated or hydrogen-terminated surfaces. We investigate the effect of the Coulomb interaction on $\epsilon_2(\omega)$ and ϵ_s at the two particle level. While Takagahara and Takeda have addressed this issue within the EMA,[4] to our knowledge this has not previously been investigated using semiempirical models. In this work we incorporate all fine-structure components, i.e., Coulomb, exchange, and spin-orbit interactions. Our treatment of the exchange interactions differs from that in a previous tight-binding study,[12] in that the electron-hole exchange interaction is unscreened and the nearest-neighbor exchange integrals are taken into account. It will be shown that the tight-binding model considered here give exchange splittings that agree qualitatively with EMA estimates for crystallites of radius ~12–14 Å, but are systematically smaller for smaller size crystallites. The tight-binding exchange splittings are in reasonable agreement with the perturbative estimates derived from a recent empirical pseudopotential calculation.[19] We

find that dark, triplet-dominated states persist in the presence of spin-orbit coupling for nanocrystal radii of up to 18 Å. The magnitude of the now approximate (i.e., as a result of the mixing induced by spin-orbit coupling) exchange splitting is somewhat reduced, but not entirely quenched, despite the tetrahedral symmetry. Comparison with experiments shows this splitting to be in good agreement with experimental exchange splittings, and the radiative lifetimes of dark and bright bands of states to be in order of magnitude agreement with the experimental values.[8]

There has been considerable controversy over the accuracy of the sp^3s^* tight-binding model used in this work.[20] This model gives band gaps that agree with luminescence experiments. The agreement is apparently fortuitous, as a more accurate tight-binding model[12] (i.e., one which gives a closer fit to silicon bulk band structure) overestimates the band gap by 0.5–1 eV over a wide range of nanocrystal sizes. A recent empirical pseudopotential calculation[21] gives band gaps in agreement with Ref. 12. The discrepancy between experiments and these models is not fully resolved. As such, no completely satisfactory tight-binding model for nanostructure silicon appears to exist, although all currently employed models do show significant improvement over EMA estimates of band gaps. In this work, we apply the sp^3s^* model to study the exciton fine structure. Our approach is in the same spirit as EMA-based calculations for excitons in nanocrystals.[4,11,13,14,22] Thus the EMA is widely used to study exciton *splittings* as functions of exciton size, despite its well-known inability to reproduce the *magnitude* of the luminescence energy. In other words, we treat the precise magnitude of the band-gap energy (which depends on the fine details of the tight-binding description) and the exciton fine structure (which is more generically a function of the quantum confinement effect) as two separate issues, the former of which will not be addressed here. Of interest here is the order of magnitude of the radiative lifetimes, and their distribution over the fine structure. While the precise values will depend on the details of the band-edge states and possibly also indirectly therefore on the band-edge positions, the latter will not necessarily affect the gross distribution of lifetimes.

Two complementary computational methods are applied in this work. First, to compute the entire absorption spectrum spanning tens of eV, we employ a real-time propagation method.[15–17,23] The spectral resolution is limited here only by the propagation length. For accurate estimation of the effects of exchange and spin-orbit interactions, high resolution is required, but only the band-gap region is pertinent. It is then more convenient to diagonalize the Hamiltonian in a restricted two-particle basis made up of electron and hole states close to the band edges.[12]

This paper is organized as follows. Section II describes the two-particle Hamiltonian, and the time-dependent and independent methods. Section III contains the results, and Sec. IV summarizes our findings with some further discussion.

II. THEORY

A. Two-particle basis set and Hamiltonian

The zeroth-order triplet/singlet electron-hole eigenstates are

$$|\Psi^{(1)}\rangle=|eh\rangle|j_s m_s\rangle=\begin{pmatrix} |eh\rangle|\alpha\alpha\rangle \\ (1/\sqrt{2})|eh\rangle(|\alpha\beta\rangle+|\beta\alpha\rangle) \\ |eh\rangle|\beta\beta\rangle \\ (1/\sqrt{2})|eh\rangle(|\alpha\beta\rangle-|\beta\alpha\rangle)\end{pmatrix}, \tag{1}$$

where e and h denote the electron (conduction band) and hole (valence band) states with single-particle eigenenergies $E_e>E_F$, $E_h<E_F$, respectively. E_F is the Fermi energy, $|j_s m_s\rangle$ is the two-particle spin portion of $|\Psi^{(1)}\rangle$, and $|\alpha\rangle$ and $|\beta\rangle$ are the one-particle spin-$\frac{1}{2}$ states. Implicit in this treatment is a first-order ''configuration-interaction'' approximation, such that multiple excitations are not explicitly considered. The two-particle Hamiltonian is derived by projecting the many-electron Hamiltonian onto the electron-hole basis in the Hartree-Fock approximation,[24,25] and is given by

$$\hat{H}=\hat{H}_o+\hat{H}_{\rm coul}+\hat{H}_{\rm ex}+\hat{H}_{\rm so}, \tag{2}$$

$$\hat{H}_o=\sum_e E_e|e\rangle\langle e|-\sum_h E_h|h\rangle\langle h|, \tag{3}$$

$$\hat{H}_{\rm coul}=-\sum_{ii'i''i'''}\sum_{\gamma\gamma'\gamma''\gamma'''}|i\gamma,i'\gamma'\rangle w(i\gamma i'''\gamma''';i'\gamma' i''\gamma'')\times\langle i'''\gamma''',i''\gamma''|, \tag{4}$$

$$\hat{H}_{\rm ex}=\delta_s\sum_{ii'i''i'''}\sum_{\gamma\gamma'\gamma''\gamma'''}|i\gamma,i'\gamma'\rangle w(i\gamma i''\gamma'';i'\gamma' i'''\gamma''')\times\langle i'''\gamma''',i''\gamma''|, \tag{5}$$

$$\hat{H}_{\rm so}=\sum_{i\gamma\gamma'\gamma''\sigma\sigma'\sigma''}|i\gamma\sigma,i\gamma''\sigma''\rangle\langle i\gamma\sigma|\lambda\hat{\mathbf{l}}_i\cdot\hat{\mathbf{s}}_i|i\gamma'\sigma'\rangle\times\langle i\gamma'\sigma',i\gamma''\sigma''|-\sum_{i\gamma\gamma'\gamma''\sigma\sigma'\sigma''}|i\gamma''\sigma'',i\gamma\sigma\rangle\times\langle i\gamma\sigma|\lambda\hat{\mathbf{l}}_i\cdot\hat{\mathbf{s}}_i|i\gamma'\sigma'\rangle\langle i\gamma''\sigma'',i\gamma'\sigma'|. \tag{6}$$

Here i is the site or atom label, γ specifies the type of orbital, σ denotes the single-electron/hole spin state, $\delta_s=2$ for the singlet states and is zero otherwise.[25] λ is the spin-orbit coupling parameter, and $\hat{\mathbf{l}}_i$ and $\hat{\mathbf{s}}_i$ are the local orbital and spin momentum operators. Note that our zeroth-order states, Eq. (1), are direct product states between spatial and spin eigenfunctions, and the spin-orbit interaction is then included as a perturbation on the single-particle spatial Hamiltonian, Eq. (3). Strictly speaking, one should diagonalize the entire single-particle Hamiltonian $\hat{H}_o+\hat{H}_{\rm so}$. We have done this, and find that the results are in excellent agreement with the perturbative treatment of spin-orbit coupling for nanocrystal sizes investigated in this work. So to facilitate comparison between the exciton effects in the presence and absence of spin-orbit coupling, and also to make it possible to compare our results with past works that neglect spin-orbit coupling,[19] we present results with the spin-orbit coupling treated perturbatively throughout. It is a good approximation to limit spin-orbit coupling to on-site interactions only.[26] Note also that only the spin portion of $|\Psi^{(1)}\rangle$ is symmetrized or anti-

symmetrized; the symmetry of the orbital wave function is taken into account by explicitly including the exchange term $\hat{H}_{\rm ex}$ in the Hamiltonian.

The integrals

$$w(i\gamma i'''\gamma''';i'\gamma' i''\gamma'')=\int dr_1\int dr_2\phi^*_{i\gamma}(r_1)\phi^*_{i'\gamma'}(r_2)\times|r_1-r_2|^{-1}\phi_{i''\gamma''}(r_2)\phi_{i'''\gamma'''}(r_1) \tag{7}$$

convolve the $1/r$ interaction with the orbital wave functions $\phi_{i\gamma}(r)$. Multiple excitations lead to screening effects, which will be treated phenomenologically by renormalizing the ''$1/r$'' interaction with a dielectric screening function $\epsilon(r)$ (Ref. 27) for the electron-hole Coulomb interaction $\hat{H}_{\rm coul}$, but not the exchange interaction $\hat{H}_{\rm ex}$.[4] This will be further discussed in Sec. II C and the Appendix.

Our application of a distance-dependent dielectric function contrasts with treatments which assume a modified continuum dielectric constant to model the screening in finite size crystallites.[3,4] Dielectric functions are also applied in Ref. 12. Even though $\epsilon(r)$ obtains from purely bulk considerations,[27] the static dielectric *constant*, ϵ_s, of a finite-sized dielectric ball derived with $\epsilon(r)$ is already substantially reduced over the bulk value.[28,29] We have also considered modifying the dielectric function for finite-sized systems.[30]

To zeroth order, i.e., ignoring $\hat{H}_{\rm coul}$, $\hat{H}_{\rm ex}$, and $\hat{H}_{\rm so}$, the exciton consists of an electron in conduction state $|e\rangle$ and a vacancy in valence state $|h\rangle$, and the total excitation energy is E_e-E_h. E_e and E_h are the eigenenergies of the Hartree-Fock single-particle wave functions in the ground many-electron state $|G\rangle$. The valence band is filled in $|G\rangle$, and E_e is then computed as the energy of a virtual orbital of such an electronic configuration.[25] $\hat{H}_{\rm coul}$ and $\hat{H}_{\rm ex}$ then lead to corrections to the many-electron excited-state energy. In the tight-binding description, the highest occupied molecular orbital (HOMO) valence state of the bulk bands consists of three degenerate p states at the Γ point.[18] Applying $\hat{H}_{\rm so}$ to these HOMO states give a spin-orbit splitting of $3\lambda/2$, which is fitted to the experimental value of 0.044 eV (Ref. 31) to yield an empirical value for λ. Just as in the single-particle energy E_h of Eq. (3), the second term in $\hat{H}_{\rm so}$, Eq. (6), pertains to the hole and carries a negative sign.

B. Dipole matrix elements

The ground-state absorption spectrum of any material is given by $\sigma_{\rm abs}(\omega)\sim\omega\epsilon_2(\omega)$, where[26]

$$\epsilon_2(\omega)=\frac{8\pi^2e^2\hbar^2}{3m_e^2\Omega}\sum_f E_{fG}^{-2}M_{fG}^2\delta(\omega-E_{fG}), \tag{8}$$

f labels the many-electron excited states, E_{fG} is the transition energy, m_e is the electron mass, Ω is the volume of the system, $M_{fG}^2=|\langle f|\hat{\mathbf{p}}|i\rangle|^2$ is the squared transition dipole matrix element between states $|f\rangle$ and $|G\rangle$, $\hat{\mathbf{p}}$ is the momentum operator, e is the electronic charge, and the transition frequency ω is expressed in units of energy (eV). In general, $\hat{\mathbf{p}}=(m_e/i\hbar)[\hat{\mathbf{r}},\hat{H}]$. In an empirical tight-binding description, $\hat{H}$ is defined by the orbital on-site energies and transfer elements between an implicit basis of localized orbitals $|i\gamma\rangle$. The operator $\hat{\mathbf{r}}$ is defined in this implicit basis by

$$\hat{\mathbf{r}}=\sum_{i\gamma}|i\gamma\rangle\mathbf{r}_i\langle i\gamma|+\sum_{i\gamma}\sum_{i'\gamma'}|i\gamma\rangle\langle i\gamma|\delta\hat{\mathbf{r}}_i|i'\gamma'\rangle\langle i'\gamma'|, \tag{9}$$

where $\delta\hat{\mathbf{r}}_i=(\hat{\mathbf{r}}-\mathbf{r}_i)$, and $\mathbf{r}_i$ is the position vector of site i. In the empirical tight-binding approach the local basis functions are never treated explicitly. Thus there is no information on the second term in Eq. (9) which requires integration of an operator which does not commute with the Hamiltonian, i.e., $\delta\hat{\mathbf{r}}_i$, over the local basis functions. If this second term is neglected, the commutator $[\hat{\mathbf{r}},\hat{H}]$ is invariant to the origin from which $\mathbf{r}_i$ is measured. Since M_{fi} is also unambiguously defined, with this approximation the bulk absorption spectrum can be calculated without any fitting or extraneous information beyond the parametrization of the tight-binding Hamiltonian.[32,33] However, the neglected contributions $\langle i\gamma|\delta\hat{\mathbf{r}}_i|i'\gamma'\rangle$, in Eq. (9) can be important.[34] For silicon, the dominant terms are those with $i=i'$, namely, $\langle i\gamma'|\delta\hat{\mathbf{r}}_i|i\gamma\rangle$. These give the on-site transition dipole matrix elements which dominate in the atomic limit. This limit is not recovered in the generic empirical tight-binding treatment.

To give a better agreement with the bulk absorption spectra obtained in experiment and in density-functional theory calculations, the additional on-site matrix elements $\langle i\gamma'|\delta\hat{\mathbf{r}}_i|i\gamma\rangle$ can be treated as fitting parameters. For the sp^3s^* parametrization, good fits are obtained with values[35–37]

$$\langle is|\delta\hat{\mathbf{r}}_i|ip_x\rangle\equiv\langle s|\delta\hat{\mathbf{r}}|p_x\rangle=0.12\mathbf{e}_x\ \text{Å},$$
$$\langle is^*|\delta\hat{\mathbf{r}}_i|ip_x\rangle\equiv\langle s^*|\delta\hat{\mathbf{r}}|p_x\rangle=1.45\mathbf{e}_x\ \text{Å}, \tag{10}$$

where $\mathbf{e}_x$ is the unit vector in the x direction. The transition dipole matrix elements for the p_y and p_z orbitals are similar. With these additional terms, $(i\hbar/m_e)M_{fG}$ is then given to zeroth order in the electron-hole interaction by

$$\langle eh|[\hat{\mathbf{r}},\hat{H}_o]|G\rangle\delta_{j_s,0}\delta_{m_s,0}=-(E_e-E_h)\langle e|\hat{\mathbf{r}}|h\rangle\delta_{j_s,0}\delta_{m_s,0}, \tag{11}$$

$$\langle e|\hat{\mathbf{r}}|h\rangle=\sum_{i\gamma\gamma'}c^*_{e;i\gamma'}c_{h;i\gamma}[\mathbf{r}_i\delta_{\gamma\gamma'}+\langle i\gamma'|\delta\hat{\mathbf{r}}_i|i\gamma\rangle], \tag{12}$$

where we used $|f\rangle=|\Psi^{(1)}\rangle|eh\rangle|j_sm_s\rangle$. In Eq. (12), $c_{e;i\gamma}$ and $c_{h;i\gamma}$ are the expansion coefficients of $|i\gamma\rangle$ for $|e\rangle$ and $|h\rangle$, with $|e\rangle=\Sigma_{i\gamma}c_{e;i\gamma}|i\gamma\rangle$, and $|h\rangle=\Sigma_{i\gamma}c_{h;i\gamma}|i\gamma\rangle$ respectively. We used the convention $\hat{H}_o|G\rangle=E_G|G\rangle=0$. In the dipole approximation, no spin-flips are allowed, and only the singlet component of $|f\rangle$ can absorb light.

In the presence of $\hat{H}_{\rm coul}$, $\hat{H}_{\rm ex}$, and $\hat{H}_{\rm so}$, the product states $|\Psi^{(1)}\rangle$ are no longer eigenfunctions of the Hamiltonian, and the eigenstates now become

$$|\Psi^{(2)}_k\rangle=\sum_{ehj_sm_s}\psi^k_{ehj_sm_s}|eh\rangle|j_sm_s\rangle, \tag{13}$$

where $\psi^k_{ehj_sm_s}$ are the two-particle expansion coefficients. Eq. (11) is replaced by

$$\langle \Psi_k^{(2)}|[\hat{\mathbf{r}},\hat{H}]|G\rangle = -E_k^{(2)} \sum_{ehj_sm_s} \psi^{k*}_{ehj_sm_s} \langle e|\hat{\mathbf{r}}|h\rangle \delta_{j_s0}\delta_{m_s0} \tag{14}$$

where $E_k^{(2)}$ is the eigenenergy for state $|\Psi_k^{(2)}\rangle$. Finally, the static dielectric constant ϵ_s is given by[3]

$$\epsilon_s = 1 + (2/\pi)\int_0^\infty d\omega\ \epsilon_2(\omega)/\omega. \tag{15}$$

C. Restricted basis set diagonalization

For finite-size crystallites, the electronic properties in the band-gap region can be readily computed by diagonalizing the Hamiltonian matrix for a small set of electron-hole two-particle states, $|\Psi\rangle = |e\rangle|h\rangle|j_sm_s\rangle$, where E_e and E_h are restricted to energies close to the band edges.[12] Here $|e\rangle$ and $|h\rangle$ are directly computed using an eigenvalue-selective Lanczos algorithm.[38,39] $\hat{H}_o$ is diagonal in the zeroth-order single-particle basis $|\Psi^{(1)}\rangle$,

$$\langle e'h';j_s'm_s'|\hat{H}_o|eh;j_sm_s\rangle = (E_e - E_h)\delta_{e,e'}\delta_{h,h'}\delta_{j_s,j_s'}\delta_{m_s,m_s'}. \tag{16}$$

The matrix elements $\langle e'h';j_s'm_s'|\hat{H}_{\rm coul}|eh;j_sm_s\rangle$ (Coulomb) and $\langle e'h';j_s'm_s'|\hat{H}_{\rm ex}|eh;j_sm_s\rangle$ (exchange) are diagonal in the spin subspace, and we therefore neglect the spin indices from now on. Expanding $|e\rangle$ and $|h\rangle$ in the local orbital basis, we obtain

$$\langle e'h'|\hat{H}_{\rm coul}|eh\rangle = \sum_{i,i',i'',i''',\gamma,\gamma',\gamma'',\gamma'''} c^*_{e';i\gamma}c^*_{h';i'\gamma'}c_{h;i''\gamma''}c_{e;i'''\gamma'''}w(i\gamma i'''\gamma''';i'\gamma' i''\gamma''), \tag{17}$$

$$\langle e'h'|\hat{H}_{\rm ex}|eh\rangle = \delta_s \sum_{i,i',i'',i''',\gamma,\gamma',\gamma'',\gamma'''} c^*_{e';i\gamma}c^*_{h';i'\gamma'}c_{e;i''\gamma''}c_{h;i'''\gamma'''}w(i\gamma i'''\gamma''';i'\gamma' i''\gamma''). \tag{18}$$

To simplify these expressions, only the two-index contributions to $w(i\gamma i'''\gamma''';i'\gamma' i''\gamma'')$ are retained. These can be identified as Coulomb and exchange terms [recall Eq. (7)]:

$$w_{\rm coul}(i\gamma,i'\gamma') = w(i\gamma i\gamma;i'\gamma' i'\gamma'), \tag{19}$$

$$w_{\rm ex}(i\gamma,i''\gamma'') = w(i\gamma i''\gamma'';i\gamma i''\gamma''). \tag{20}$$

Thus we neglect terms with more than two distinct orbitals, in accordance with Ref. 12. The higher-order overlaps are small because the wave functions are (assumed) orthonormal. The principal corrections to this assumption give rise to the ''dipole''-like terms,[25] which are smaller in magnitude and can be neglected (see the Appendix). Equations (17) and (18) then reduce to

$$\begin{aligned}\langle e'h'|\hat{H}_{\rm coul}|eh\rangle &= -\sum_{ii'\gamma\gamma'} c^*_{e';i\gamma}c^*_{h';i'\gamma'}c_{h;i'\gamma'}c_{e;i\gamma}w_{\rm coul}(i\gamma,i'\gamma') \\ &\quad -\sum_{\langle ii'\rangle\gamma\gamma'}{}' c^*_{e';i\gamma}c^*_{h';i'\gamma'}c_{h;i\gamma}c_{e;i'\gamma'}w_{\rm ex}(i\gamma,i'\gamma') \\ &\quad -\sum_{\langle ii'\rangle\gamma\gamma'}{}' c^*_{e';i\gamma}c^*_{h';i\gamma}c_{h;i'\gamma'}c_{e;i'\gamma'}w_{\rm ex}(i\gamma,i'\gamma'),\end{aligned} \tag{21}$$

$$\begin{aligned}\langle e'h'|\hat{H}_{\rm ex}|eh\rangle &= \Bigg[\sum_{\langle ii'\rangle\gamma\gamma'} c^*_{e';i\gamma}c^*_{h';i'\gamma'}c_{h;i'\gamma'}c_{e;i\gamma}w_{\rm ex}(i\gamma,i'\gamma') \\ &\quad +\sum_{\langle ii'\rangle\gamma\gamma'}{}' c^*_{e';i\gamma}c^*_{h';i\gamma}c_{h;i'\gamma'}c_{e;i'\gamma'}w_{\rm ex}(i\gamma,i'\gamma') \\ &\quad +\sum_{ii'\gamma\gamma'}{}' c^*_{e';i\gamma}c^*_{h';i'\gamma'}c_{h;i\gamma}c_{e;i'\gamma'}w_{\rm coul}(i\gamma,i'\gamma')\Bigg]\delta_s.\end{aligned} \tag{22}$$

The restricted (primed) sums denote the constraint $(i\gamma) \neq (i'\gamma')$. As mentioned in Sec. II A, and discussed in some detail in the Appendix, the ''$1/r$'' interaction in the electron-hole Coulomb interaction, Eq. (17), is to be screened, while that in the electron-hole exchange interaction, Eq. (18), is not. Thus all integrals entering Eq. (21) are screened, while those in Eq. (22) are not. We use the dielectric function of Ref. 27 together with the Ohno formula[40,41] and on-site renormalizations described in the Appendix to approximate the screening.

In principle, nearest-neighbor $w_{\rm ex}(i\gamma,i'\gamma')$ integrals in the local orbital basis can contribute significantly to the electron-hole exchange matrix elements $\langle e'h'|\hat{H}_{\rm ex}|eh\rangle$, especially in II-VI semiconductors such as cadmium selenide, where the electron and hole have small on-site overlaps.[34] Beyond the nearest neighbors, $w_{\rm ex}(i\gamma,i'\gamma')$ decreases exponentially and can be neglected. Both the multi-band EMA treatment of Ref. 4 and the previous tight-binding calculation of Ref. 12 truncated the exchange interaction more severely than this. In the EMA treatment the exchange interaction is approximated by a δ-function interaction,[4] while the tight-

binding calculation included only the on-site exchange integrals.[12] Unfortunately in the latter calculation the exchange terms were also incorrectly screened, as pointed out by Takagahara and Takeda.[4] A recent empirical pseudopotential calculation[19] incorporated the long-range component of the exchange interaction. However, in contrast to Refs. 4 and 12 which are both nonperturbative configuration interaction treatments like the calculations presented here, Ref. 19 only deals with both Coulomb and exchange energies in perturbation theory for relatively small nanocrystals and also neglected spin-orbit coupling, making quantitative comparison with the truncated exchange calculations difficult. Therefore in Sec. III B we specifically examine the effect of the nearest-neighbor exchange terms.

The spin-orbit coupling in Eq. (6) is straightforwardly computed in the local orbital basis,

$$\langle e'h'j_s'm_s'|\hat{H}_{\rm so}|ehj_sm_s\rangle=\lambda\,\delta_{hh'}\sum_{i,\gamma,\gamma'}c^*_{e';i\gamma'}c_{e;i\gamma}\langle i\gamma'|\hat{\mathbf{l}}_i|i\gamma\rangle\langle j_s'm_s'|\hat{\mathbf{s}}_i|j_sm_s\rangle-\lambda\,\delta_{ee'}\sum_{i,\gamma,\gamma'}c^*_{h';i\gamma'}c_{h;i\gamma}\langle i\gamma'|\hat{\mathbf{l}}_i|i\gamma\rangle\times\langle j_s'm_s'|\hat{\mathbf{s}}_i|j_sm_s\rangle. \tag{23}$$

With the inclusion of Coulomb, exchange, and spin-orbit couplings, the two-particle Hamiltonian matrix becomes the supermatrix

$$\mathcal{H}=\begin{pmatrix}\mathcal{H}_{\rm coul}+\mathcal{H}_{\rm so}^{11;11} & \mathcal{H}_{\rm so}^{11;10} & \mathcal{H}_{\rm so}^{11;1\bar{1}} & \mathcal{H}_{\rm so}^{11;00}\\ \mathcal{H}_{\rm so}^{10;11} & \mathcal{H}_{\rm coul}+\mathcal{H}_{\rm so}^{10;10} & \mathcal{H}_{\rm so}^{10;1\bar{1}} & \mathcal{H}_{\rm so}^{10;00}\\ \mathcal{H}_{\rm so}^{1\bar{1};11} & \mathcal{H}_{\rm so}^{1\bar{1};10} & \mathcal{H}_{\rm coul}+\mathcal{H}_{\rm so}^{1\bar{1};1\bar{1}} & \mathcal{H}_{\rm so}^{1\bar{1};00}\\ \mathcal{H}_{\rm so}^{00;11} & \mathcal{H}_{\rm so}^{00;10} & \mathcal{H}_{\rm so}^{00;1\bar{1}} & \mathcal{H}_{\rm coul}+\mathcal{H}_{\rm ex}+\mathcal{H}_{\rm so}^{00;00}\end{pmatrix}, \tag{24}$$

where the elements are each $(M_e\times M_h)$ by $(M_e\times M_h)$ matrices in the $|e\rangle|h\rangle$ space, and the superscripts in $\mathcal{H}_{\rm so}^{j_s'm_s';j_sm_s}$ are the spin quantum numbers. M_e and M_h are the number of conduction and valence states taken in the restricted basis. We only consider expansions with $M=M_e=M_h$ here. We have found that $M=12$ is sufficient to converge the first few two-particle states close to the band edge. $\mathcal{H}$, augmented with the single-particle energies, is diagonalized, and the two-particle absorption spectrum is obtained via Eqs. (8) and (14).

D. Real-time propagation

To compute the complete absorption spectrum and related properties such as the dielectric constant with the time-independent method, it is necessary to know the entire $|{\rm eh}\rangle$ basis set. The dimension of the two-particle Hamiltonian matrix scales as N^2, where N is the number of atoms in the nanocluster. With the sp^3s^* parametrization, the largest crystallite that can be treated in this way is $N=41$. For larger clusters the spectral properties can be studied by Fourier transforming the real-time dipole-dipole correlation function.[42] Starting from Eq. (8), and using $\hat{\mathbf{p}}=(m_e/i\hbar)[\hat{\mathbf{r}},\hat{H}]$,

$$\begin{aligned}\epsilon_2(\omega)&=\frac{8\pi^2e^2}{3\Omega}\sum_f\mathbf{r}_{Gf}\cdot\mathbf{r}_{fG}\delta(\omega-E_{fG})\\&=\frac{8\pi e^2}{3\Omega\hbar}\int_0^\infty dt\ {\rm Re}\ e^{i\omega t}\sum_f\langle G|\hat{\mathbf{r}}e^{-iE_{fG}t/\hbar}|f\rangle\cdot\langle f|\hat{\mathbf{r}}|G\rangle\\&=\frac{8\pi e^2}{3\Omega\hbar}\int_0^\infty dt\ {\rm Re}\ e^{i\omega t}\langle G|\hat{\mathbf{r}}\cdot e^{-i\hat{H}t/\hbar}\hat{\mathbf{r}}|G\rangle,\end{aligned} \tag{25}$$

where the convention $\hat{H}|G\rangle=E_G|G\rangle=0$ remains in force. This suggests the following procedure: (a) compute the vector $|\Psi'\rangle=\hat{\mathbf{r}}|G\rangle=\Sigma_{eh}\langle e|\hat{\mathbf{r}}|h\rangle|eh\rangle$ in some basis; (b) apply the two-particle propagator $e^{-i\hat{H}t/\hbar}$, $0\leqslant t<t_{\rm max}$; (c) compute and store the overlap $C(t)$ at each time t,

$$C(t)=\langle G|\hat{\mathbf{r}}\cdot e^{-i\hat{H}t/\hbar}\hat{\mathbf{r}}|G\rangle;$$

and (d) Fourier transform $C(t)$. This yields $\epsilon_2(\omega)$, Eq. (8), and hence the absorption spectrum $\sigma_{\rm abs}(\omega)\sim\omega\epsilon_2(\omega)$. We can then obtain the static dielectric constant with the effect of the Coulomb interaction incorporated nonperturbatively, from Eqs. (15) and (25),

$$\epsilon_s=1-\frac{16\pi e^2}{3\Omega\hbar}\int_0^\infty dt\ {\rm Im}\langle G|\hat{\mathbf{r}}\cdot e^{-i\hat{H}t/\hbar}\hat{\mathbf{r}}|G\rangle. \tag{26}$$

In keeping with the single excitation approximation, a projection operator $\hat{P}=\Sigma_{eh}|eh\rangle\langle eh|$ is applied, $\hat{H}\rightarrow\hat{P}\hat{H}\hat{P}$, so that the Hamiltonian does not scatter conduction and valence states into each other.

The resolution of the spectrum is inversely proportional to length of propagation $t_{\max}$, and is set at 50 meV in this work. On this energy scale, spin-orbit splittings are unresolved, $\hat{H}_{\rm so}$ can be neglected, and singlet and triplet states are therefore decoupled. For simplicity, we also neglect $\hat{H}_{\rm ex}$, whose contribution is typically less than 25% of the Coulomb interaction, and set $\hat{H}=\hat{H}_o+\hat{H}_{\rm coul}$. In $\hat{H}_{\rm coul}$ we also neglect terms $w_{\rm ex}(i\gamma,i'\gamma')$, consistent with this level of approximation.

The two-particle vector $\hat{\mathbf{r}}|{\rm eh}\rangle$ is evolved in time using a series of short-time propagators,

$$e^{-i\hat{P}\hat{H}\hat{P}t_{\max}/\hbar}=[e^{-i\hat{P}\hat{H}\hat{P}dt/\hbar}]^N,$$
$$e^{-i\hat{P}\hat{H}\hat{P}dt/\hbar}\approx e^{-i\hat{P}\hat{H}_o\hat{P}dt/\hbar}e^{-i\hat{P}\hat{H}_{\rm coul}\hat{P}dt/\hbar}+O(dt^2), \tag{27}$$

where $N=t_{\max}/dt$ is the Trotter partition number.[23] It is convenient to propagate in the electron-hole orbital basis, $\{|i\sigma,i'\sigma'\rangle\}$. While $\hat{H}_{\rm coul}$ mixes valence and conduction states, it only provides a weak perturbation in the strong confinement regime, and the scattering between valence and conduction states should be small. For greater efficiency, as will become clear below, it is advisable to neglect the action of the projection operators $\hat{P}$ on $\hat{H}_{\rm coul}$.[29,43] The validity of this approximation for Si nanosystems will be demonstrated below. Under the action of the approximate $\hat{H}$, we have then

$$\hat{P}\hat{H}_o\hat{P}|i\gamma,i'\gamma'\rangle=\sum_{i''\gamma''}[T^e_{i''\gamma''i\gamma}|i''\gamma'',i'\gamma'\rangle - T^h_{i''\gamma'',i'\gamma'}|i\gamma,i''\gamma''\rangle] \tag{28}$$

$$\hat{H}_{\rm coul}|i\gamma,i'\gamma'\rangle=w_{\rm coul}(i\gamma,i'\gamma')|i\gamma,i'\gamma'\rangle, \tag{29}$$

where

$$T^e_{i''\gamma''i\gamma}=\sum_e E_e\langle i''\gamma''|e\rangle\langle e|i\gamma\rangle,$$
$$T^h_{i''\gamma''i'\gamma'}=\sum_h E_h\langle i''\gamma''|h\rangle\langle h|i'\gamma'\rangle. \tag{30}$$

The single-particle eigenstates and eigenenergies are needed as input in this formulation. They are obtained here from diagonalizing the tight-binding Hamiltonian. Using a ''hyper-checkerboard'' decomposition,[23] which is a generalization of the standard checkerboard decomposition[44] to full matrices, the short-time propagator becomes

$$e^{-i\hat{H}dt/\hbar}=\hat{U}^e_o(dt)\hat{U}^h_o(dt)\hat{U}_{\rm coul}(dt),$$
$$\hat{U}^e_o(dt)=\Pi_{\{(i\gamma)\leq(i''\gamma'');i'\gamma'\}}\hat{u}^e(i\gamma,i''\gamma'';i'\gamma'),$$
$$\hat{U}^h_o(dt)=\Pi_{\{(i'\gamma')\leq(i''\gamma'');i\gamma\}}\hat{u}^h(i'\gamma',i''\gamma'';i\gamma),$$
$$\hat{U}_{\rm coul}(dt)=\Pi_{\{i\gamma,i'\gamma'\}}\hat{u}_{\rm coul}(i\gamma,i'\gamma'), \tag{31}$$

where further $O(dt^2)$ corrections have been neglected. The action of the binary evolution operators $\hat{u}$ on a two-particle state in the site local basis is given exactly by

$$\hat{u}_{\rm coul}(i\gamma,i'\gamma')|i\gamma,i'\gamma'\rangle = \cos[w_{\rm coul}(i\gamma,i'\gamma')dt/\hbar]|i\gamma,i'\gamma'\rangle - i\,\sin[w_{\rm coul}(i\gamma,i'\gamma')dt/\hbar]|i\gamma,i'\gamma'\rangle,$$
$$\hat{u}^e(i\gamma,i''\gamma'';i'\gamma')|i\gamma,i'\gamma'\rangle = \cos(T^e_{i''\gamma''i\gamma}dt/\hbar)|i\gamma,i'\gamma'\rangle - i\,\sin(T^e_{i''\gamma''i\gamma}dt/\hbar)|i''\gamma'',i'\gamma'\rangle, \tag{32}$$
$$\hat{u}^h(i'\gamma',i''\gamma'';i\gamma)|i\gamma,i'\gamma'\rangle = \cos(T^h_{i''\gamma''i'\gamma'}dt/\hbar)|i\gamma,i'\gamma'\rangle - i\,\sin(T^h_{i''\gamma''i'\gamma'}dt/\hbar)|i\gamma,i''\gamma''\rangle.$$

Each of these binary evolutions constitutes one elementary step in the hypercheck-board propagation. $\hat{U}_{\rm coul}(dt)$ is diagonal in the $|i\gamma,i'\gamma'\rangle$ basis, and so provides only a phase factor, to be evaluated M^2 times, where M is the total number of orbital basis functions defined earlier. In contrast, multiplying $\hat{\mathbf{r}}|eh\rangle$ by $\hat{U}^e_o(dt)$ and $\hat{U}^h_o(dt)$ are both M^3 operations. These therefore constitute the limiting steps in the algorithm. An alternative basis set is $\{|eh\rangle\}$. $\hat{H}_o$ is diagonal in this basis, but computing $\hat{U}_{\rm coul}|eh\rangle$ now becomes an M^4 operation. (The same would apply to the action of the projection operators $\hat{P}$ on $\hat{H}_{\rm coul}$, which we have neglected here.) The orbital basis set is therefore more efficient.

III. RESULTS

A. Full absorption spectra: real-time calculation

Figures 1–3(a) show the real-time two-particle absorption spectra $\epsilon_2(\omega)$ for $N=41$-, 83-, and 147-atom nanocrystals. The nanocrystals are constructed by sequentially adding shells about a central atom, and therefore have tetrahedral symmetry. These crystallites have the sp^3s^* parametrization of Ref. 18 and have truncated surfaces, i.e., dangling orbitals are eliminated from the basis. A 30-meV half-width filter has been applied. Figure 1(a) also plots the two-particle spectrum obtained from diagonalizing the entire 41-atom, two-particle Hamiltonian (Sec. II C), the largest such Hamiltonian which can be fully diagonalized. The real-time propagation and diagonalization results are in very good agreement, demonstrating that one can with validity neglect $\hat{P}$ in the short-time propagator in Eqs. (29) and (31) for these Si nanocrystals.

The lowest-energy structure is the exciton peak. It is progressively redshifted as the cluster size increases and quantum confinement effect decreases. The time-*independent* calculation (Sec. III B) predicts first peaks at frequencies 3.05, 2.58, and 2.24 eV for the 41-, 83-, and 147-atom nanocrystals respectively. They compare well with the first peak at 3.06 eV in Fig. 1, and the first shoulder at 2.60 eV in Fig. 2, respectively. The first exciton structure of the 147-atom cluster is not resolved. The single-particle absorption spectra are shown in Figs. 1–3(b). The lowest non-interacting two-

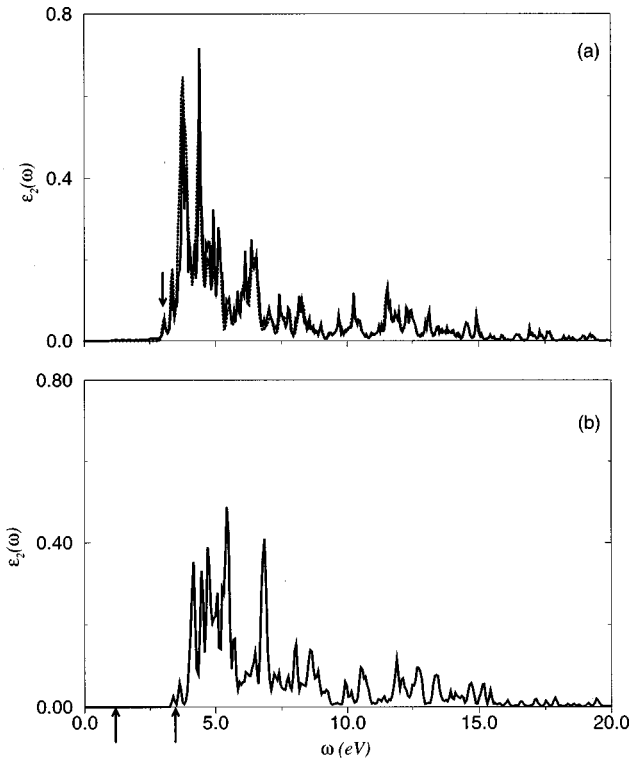

FIG. 1. $\epsilon_2(\omega)$ for the 41-atom (5.8-Å radius) Si nanocrystal with truncated surface, in arbitary units. (a) With Coulomb interaction. Solid line—real-time calculation; dotted line—diagonalization of two-particle Hamiltonian. The arrow indicates the exciton peak. (b) Without Coulomb interaction (i.e., diagonalization of a single-particle Hamiltonian). The arrows indicate the indirect and direct bulk band gap, 1.17 and 3.43 eV, respectively.

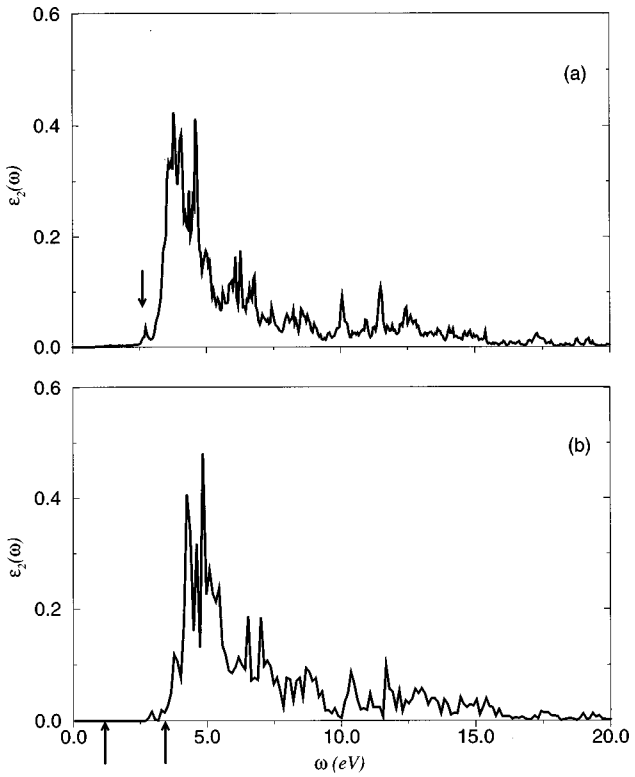

FIG. 2. $\epsilon_2(\omega)$ for the 83-atom (7.35-Å radius) Si nanocrystal with truncated surface. (a) With Coulomb interaction. (b) No Coulomb interaction. The symbols are as in Fig. 1.

particle energy levels are at 3.36, 2.79, and 2.41 eV, respectively, for the three sizes. The Coulomb corrections to the exciton energy are therefore approximately 0.33, 0.20, and 0.17 eV. These corrections were shown previously to be in good agreement with perturbative estimates.[15,16] They increase with decreasing nanocrystal size, due to the increased overlap between the electron and hole wave functions.

Compared to the single-particle results, the two-particle spectra are almost uniformly redshifted by the Coulomb corrections to the band edge energy, i.e., by roughly 0.3, 0.2, and 0.15 eV over the whole energy range. This implies that the Coulomb interaction is perturbative over most of the spectrum. The strong peak at 4–5 eV is the exception. Large changes in the spectral envelope are observed, with absorption intensities shifting to lower frequencies by up to 1 eV. The zeroth-order states are extensively mixed in this high density-of-states regime, and perturbation theory is no longer valid. Oscillator strengths are large among electron and hole wave functions that exhibit large overlap. Not coincidentally, it is these states that also experience the strongest Coulomb interactions. This explains the qualitative changes in spectral line shape in this region.

The two-particle spectra for the three sizes have similar shapes, indicating that a convergence to bulklike behavior is rapidly obtained even for clusters of 41–147 atoms. High-energy absorption spectra ($\omega > 3$ eV) for small crystallites have been reported, and this rapid convergence is also in evidence in that experimental work.[45] As silicon is an

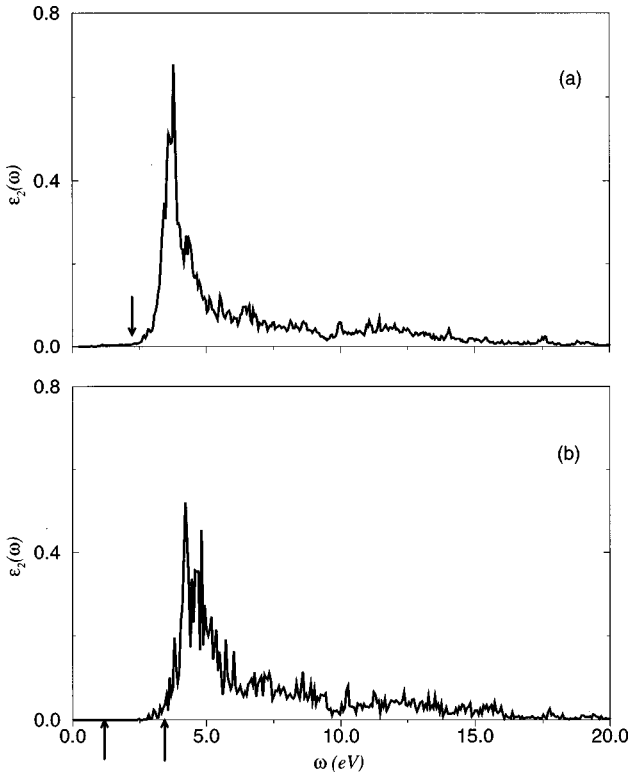

FIG. 3. $\epsilon_2(\omega)$ for the 147-atom (8.9-Å radius) Si nanocrystal with truncated surface. (a) With Coulomb interaction. (b) No Coulomb interaction. The symbols are as in Fig. 1. In panel (a), the exciton peak (arrow) is not resolved.

TABLE I. Static dielectric constants for sp^3s^* parametrized nanocrystals. ϵ_s^c: surface-truncated crystallites with Coulomb interaction, Eq. (26); ϵ_s^0: surface-truncated crystallites, without Coulomb interaction, Eq. (15); ϵ_s^H: hydrogen-terminated crystallites, without Coulomb interaction, Eq. (15).

Cluster radius (Å)	5.8	7.35	8.9
ϵ_s^c	7.64	8.28	9.54
ϵ_s^0	6.86	7.57	8.63
ϵ_s^H	8.89	9.39	10.28

indirect-gap material, at $T=0$ there is no bulk absorption at the band gap energy of 1.17 eV, and the onset of bulk absorption is at the direct-band gap value of 3.43 eV. However, in the finite-size crystallites there is absorption below 2 eV because of the quantum confinement induced overlap of the electron and hole wave functions in reciprocal space.[15,46] The spectral shift due to the Coulomb correction [compare Figs. 1(a) and Fig. 1(b)] clearly enhances this increase in absorption. Thus, despite being perturbative in magnitude, the Coulomb term has a significant effect on the sub-direct-gap absorption.

Table I tabulates the values of the static dielectric constants ϵ_s obtained for crystallites with and without the Coulomb interaction included, and with various surface terminations. (a) ϵ_s^c: surface-truncated crystallites with Coulomb interactions, computed via Eq. (26); (b) ϵ_s^o: surface-truncated crystallites, without Coulomb interactions, computed via Eq. (15); and (c) ϵ_s^{H}: hydrogen-terminated crystallites, also without Coulomb interactions, computed via Eq. (15). The general trend of decreasing ϵ_s with decreasing cluster size already noted in Ref. 3, and expected from the simple consideration of the effect of finite-size confinement on a distance-dependent dielectric function discussed above (Sec. I and Ref. 30), is evident in all three instances. Additional trends are also apparent here. We see that $\epsilon_s^c-\epsilon_s^o\sim 1$, but that ϵ_s^c is systematically larger by $\sim 10\%$. Thus the electron-hole attraction, neglected in ϵ_s^o, gives rise to a noticeable increase in ϵ_s. A similar effect was seen for very small crystallites in the EMA calculations of Ref. 4, but here it is evident even for the 8.9-Å-radius crystallite. The second systematic feature is that $\epsilon_s^{\mathrm{H}}-\epsilon_s^o\sim 2$. This is of the same order as the surface contribution estimated in Ref. 3 for spherical clusters of similar size, and demonstrates that the surface termination can strongly affect the screening, although the main contribution to the reduction in ϵ_s below its bulk value ($\epsilon_s=11.4$) does come from the confinement. In addition to recognizing the size dependence of dielectric screening in nanocrystals, it is clearly important to realize also that values of ϵ_s computed using different approximations are strongly parametrization dependent.[3]

B. Fine structure near band edge: time-independent calculation

In the absence of spin-orbit coupling, the Hamiltonian matrix in Eq. (24) is block diagonal, and the two-particle states are unambiguously singlets and triplets. Figure 4 plots the Coulomb and exchange energies which are obtained with a restricted basis diagonalization of the singlet and triplet

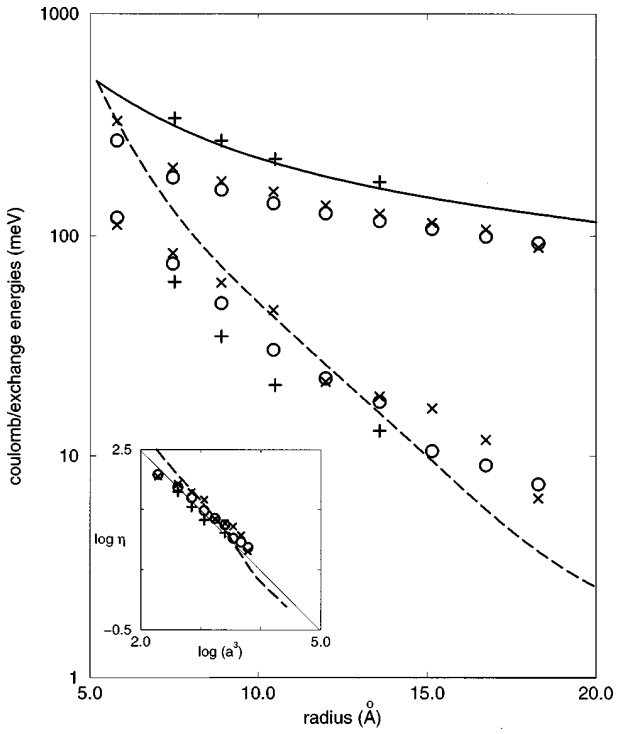

FIG. 4. Coulomb and exchange energies for two tight-binding cluster models. Crosses—sp^3s^* parameters with truncated surface; circles—sp^3s^* parameters with a hydrogen-terminated surface. The upper sets of data are Coulomb energies, while the lower sets pertain to exchange. The solid and dashed lines are the Coulomb and exchange interactions calculated with multiband EMA in Ref. 4. Pluses refer to pseudopotential perturbative results of Ref. 3. Inset: exchange energies (η in meV) vs a^3, where a is the radius on a base 10 logarithmic scale. Symbols and dashed line as in the main panel. The solid line shows the strong confinement scaling behavior $\eta\propto a^{-3}$ predicted by simple EMA.

manifolds, respectively. The Coulomb energy is defined as the difference between the lowest triplet two-particle state and the single-particle band gap, while η, the exchange energy, is the splitting between the lowest singlet and triplet levels. Two sets of data are shown, corresponding to two different surface terminations: (a) sp^3s^* with truncated surface (crosses), and (b) sp^3s^* with hydrogen-terminated surface (circles). The Si-H parameters are taken from Ref. 16. These results were obtained with nearest-neighbor exchange terms in the local orbital basis included. Also shown are the EMA estimates of Ref. 4 (solid and dashed lines) and the empirical pseudopotential results from Ref. 19 (pluses).

We first discuss the Coulomb energies. These are relatively insensitive to the incorporation of nearest-neighbor exchange terms in the local orbital basis: only a 2% or less change results from adding these terms to the calculation. The Coulomb energies computed here are 35% smaller than those derived from the multiband EMA treatment (solid line).[4] A significant overestimation of Coulomb energies by simple (single band) EMA has been noted recently in a comparison of perturbative estimates between EMA and pseudopotential calculations,[19] where the difference was assigned to errors in the EMA wave functions, both at the local and envelope-function level. Given this, the similarity evident in Fig. 4 between the perturbative pseudopotential results of

Ref. 19 with the multiband EMA results of Ref. 4 is very interesting. Since the two calculations appear to use the same size-dependent dielectric constant, this agreement, which was not noted in Ref. 19, would appear to derive from the multiband nature of Ref. 4. Now comparing our current tight-binding results with these prior calculations, we note first that the Coulomb energies do not appear to be sensitive to the small differences in effective dielectric constant for the two different surface terminations (a) and (b) (see Table I), and thus the smaller Coulomb energy obtained here is probably not attributable to the use of the dielectric function rather than the simpler dielectric constant description of Refs. 4 and 19. The lower values we find appear to derive rather from the use of the Ohno formula to approximate off-site Coulomb integrals, rather than a point-charge approximation as was used in Ref. 12 (see the Appendix). The latter gives systematically larger values of all off-site Coulomb integrals, and therefore results in a larger Coulomb energy, since this is dominated by the Coulomb integrals (unlike the exchange energy, as discussed in the Appendix).

The exchange energies of the truncated (a) and hydrogen-terminated (b) nanocrystals differ somewhat more than the Coulomb energies, by approximately 10–40%, but the difference is not systematic. It appears to arise from subtle differences in the confinement of the electron and hole wave functions to which the exchange energy is more sensitive than the Coulomb energy. While not excessively large, this nevertheless indicates that the surface has a noticeable effect on the exciton fine structure, even for nanocrystals of radius 15 Å, despite the fact that the band-edge wave functions have virtually no population in the hydrogen ligand orbitals themselves. At nanocrystal radius $\sim 12-14$ Å, the tight binding configuration interaction energies are in reasonable agreement with the multiband EMA results of Ref. 4. At smaller sizes the EMA exchange energies are markedly larger. When the crystallite radius drops below 5 Å, the EMA erroneously predicts that exchange energies exceed the Coulomb energies. Therefore such treatment is not adequate for small crystallites. In the inset of Fig. 4 we show a comparison with the $\eta \propto a^{-3}$ scaling behavior predicted by simple EMA in strong confinement, where a is the linear dimension of the nanocrystals. While the tight-binding results show this scaling to be valid to a good approximation, the multiband EMA results of Ref. 4 do not show $\eta \propto a^{-3}$ scaling at all over the size range shown in Fig. 4. As mentioned above, the data shown in Fig. 4 were computed with both on-site and nearest-neighbor exchange integrals. The resulting exchange splittings agree with the perturbative results of Ref. 19 to within 25–40% (Fig. 4). Omitting the nearest-neighbor exchange integrals decreases the bare exchange interactions by roughly a factor of 2.

Spin-orbit coupling mixes singlet and triplet states. In Figs. 5–8 we plot the fractional singlet character, defined as $|\langle f|00\rangle|^2$, for each exciton state $|f\rangle$ of hydrogen-coated nanocrystals with the sp^3s^* parameterization, containing up to $N=1285$ atoms. Also shown are the radiative recombination rates for each state,[47]

$$1/\tau_{fG}=\frac{4ne^2E_{fG}^3|\mathbf{r}_{fG}|^2}{3\hbar^4c^3}, \tag{33}$$

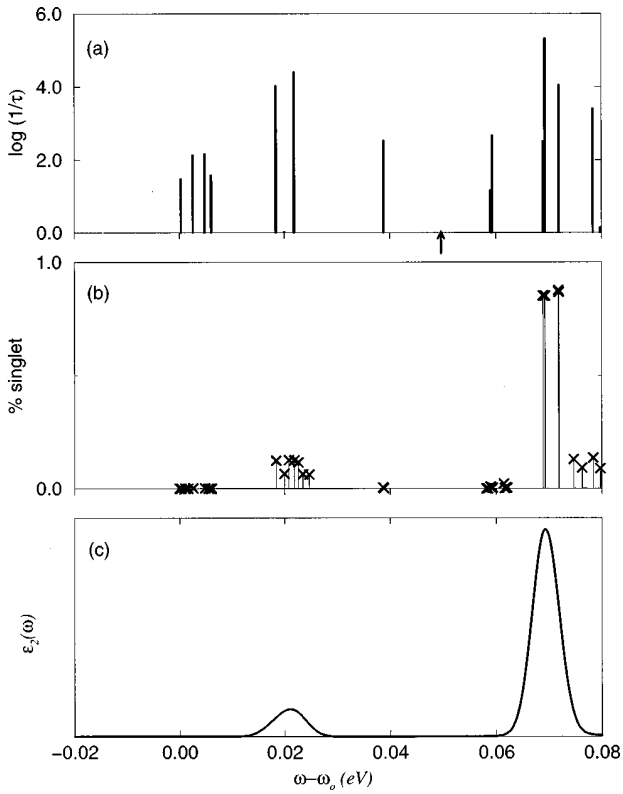

FIG. 5. Fine structure for the 147-atom (8.9-Å radius) hydrogen-terminated Si nanocrystal. From top to bottom: (a) logarithm of radiative recombination rate, $1/\tau$; (b) percent singlet character; (c) $\epsilon_2(\omega)$ (arbitrary units). Shorter-lived states have larger values of $\log(1/\tau)$. The line spectrum in (c) has been broadened with a Gaussian function of half-width 2.5 meV. Frequencies are measured with respect to the lowest two-particle level, i.e., $\omega_o=1.907$ eV. $\eta=0.050$ eV (arrow) for this nanocrystal.

where $n=2.6$ is the bulk refractive index, and c is the speed of light. The radiative lifetime, τ_{fG}, is thus inversely proportional to the oscillator strength. The density of states is quite complex, with many states lying extremely close to each other, their degeneracies now lifted by the small spin-orbit couplings. Nevertheless, in all cases, the first few levels are dark and predominantly triplets. States with appreciable singlet character are blueshifted with respect to the band edge by roughly η, which therefore retains its significance as an exchange splitting. This is particularly apparent in the broadened absorption spectra, which exhibit first peaks or shoulders between $\omega_o+0.5\eta$ and $\omega_o+\eta$. These results contrast with Ref. 12, which finds that, for high-symmetry crystallites, pure triplet states are completely destroyed by spin-orbit coupling. We attribute the difference to the fact that, unlike Ref. 12, we do not screen the electron-hole exchange interaction[4] (see the Appendix), and that we also incorporate the contributions from nearest-neighbor exchange integrals. As a result, we obtain larger values of η, which helps preserve the triplet character of band-edge states. Note that because of the mixing due to spin-orbit coupling, the first state with appreciable oscillator strength does not lie at exactly $\omega_o+\eta$, in contrast to the assumption implicit in the perturbative treatment of Ref. 19, which omitted the spin-orbit coupling.

The line spectra in Figs. 5–8(a) show that the band-edge

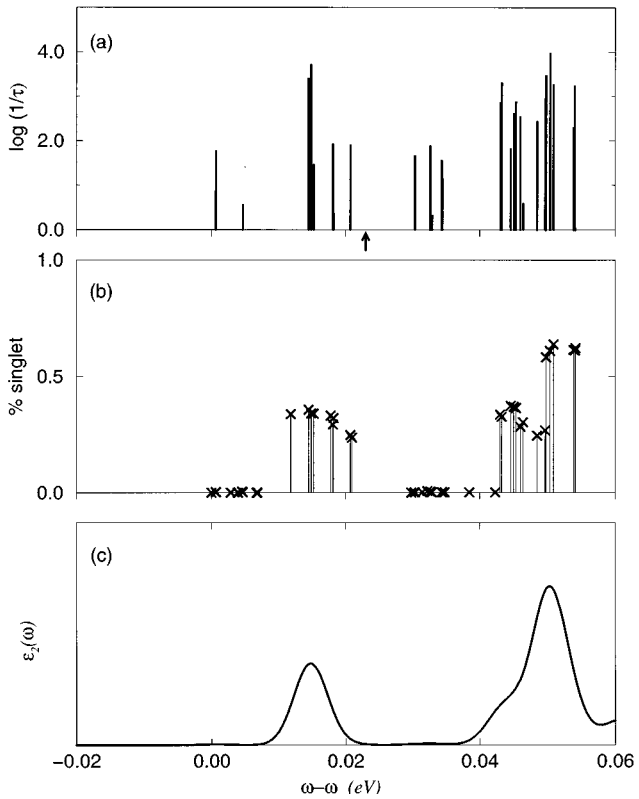

FIG. 6. Fine structure for the 363-atom (12.0-Å radius) hydrogen-terminated Si nanocrystal. Symbols are the same as in Fig. 5. See Fig. 5 for definitions. $\omega_o = 1.627$ eV and $\eta = 0.023$ eV for this nanocrystal.

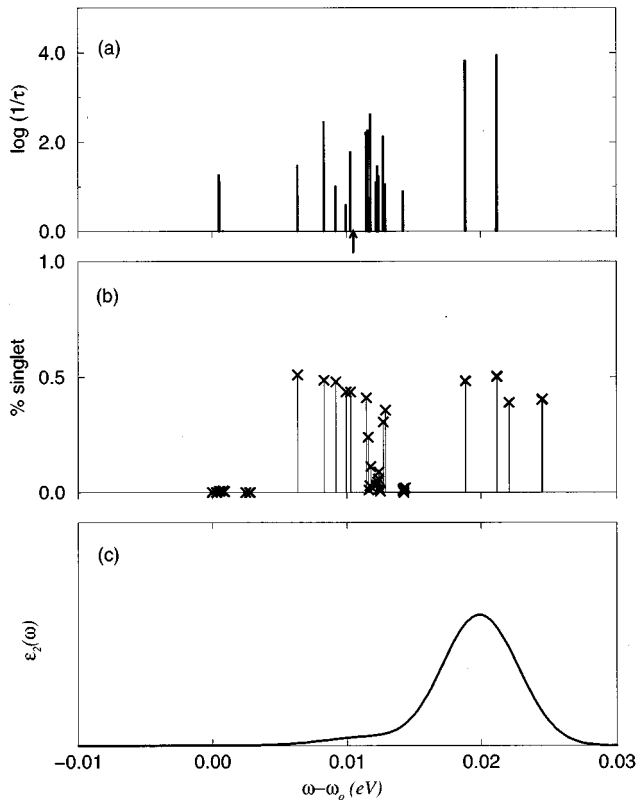

FIG. 7. Fine structure for the 729-atom (15.2-Å radius) hydrogen-terminated Si nanocrystal. Symbols are the same as in Fig. 5. See Fig. 5 for definitions. $\omega_o = 1.472$ eV and $\eta = 0.011$ eV for this nanocrystal.

triplets have lifetimes τ_{fG} which are roughly 1–3 orders of magnitude larger than those of the bright states. This indicates that a two- (or in some cases, three-) state model[7] is adequate, even for ''spherical'' crystallites. The radiative lifetimes for the low lying bright states at the band edge are $10^{-6}-10^{-3}$ s. In Fig. 9(a), we further analyze the lifetimes by calculating the recombination rates τ_{fG}^{-1} for two or three prominent, well-separated peaks or shoulders, at frequencies $(\omega-\omega_o)$ less than or of order η. These are categorized as ''bright'' or ''dark'' states, depending on whether their energies are at least $\sim 0.4\eta$ above the band edge or not. The plots verify that the lifetimes of these two categories lie in two separate bands, and are separated by factors of 10^1-10^3. Our bimodal distribution of τ_{fG}^{-1} is qualitatively similar to the results of Ref. 12 for *nonspherical* nanocrystals. However the decay rates obtained in Ref. 12 are consistently smaller, and the lifetimes correspondingly longer (see also comparison with experiment below). The bands would collapse into one if the exchange interaction $\hat{H}_{\rm ex}$ were omitted. The line spectra for surface-truncated crystallites (not shown) are qualitatively similar. However, for large (>12 Å radius) crystallites, the radiative lifetimes for surface-truncated crystallites are about ten times larger than their hydrogen-coated counterparts [see Fig. 9(b)—τ^{-1} is systematically smaller], and the demarcation into bright and dark bands is less obvious. For both surface terminations, the oscillator strengths generally decrease as the nanocrystal increases in size, in agreement with the predictions of EMA and with experiments.[1,2,4]

Comparison between our theoretical and the experimental[8,48] exchange splittings for the hydrogen-terminated crystallites is made in Fig. 10(a), and between theoretical and experimental[8] radiative lifetimes in Fig. 10(b). The exchange splittings for crystallites with radii $\geqslant 8.9$ Å are seen to agree with the ''variable temperature τ'' estimates of Ref. 8. The latter are obtained by fitting the exchange splitting needed to reproduce the temperature dependence of the radiative lifetimes to a two-level model.[8] These estimates are larger than the Stokes shifts observed in photoluminescence measurements (onset measurements). Figure 10(b) shows that, for this size range, our calculated radiative lifetimes for both bright and dark bands are generally within an order of magnitude of the experimental values. The improved agreement relative to the prior tight-binding study which found lifetimes between 10^1 and 10^3 times that of the experimental values[12] is assigned to the improved treatment of exchange. For the smaller crystallites, oscillator strengths of the band-edge states can become strongly dependent on crystallite size and shapes, yielding a large scatter in radiative lifetimes.[4,46] Quantitative comparisons should therefore not be made in the present context.

IV. CONCLUSION

In this paper, we have demonstrated that the real-time propagation method previously used to study the density of states and exciton binding in nanocrystals[15–17,23] can be adapted to compute the entire absorption spectrum and related properties such as the static dielectric constant. Non-

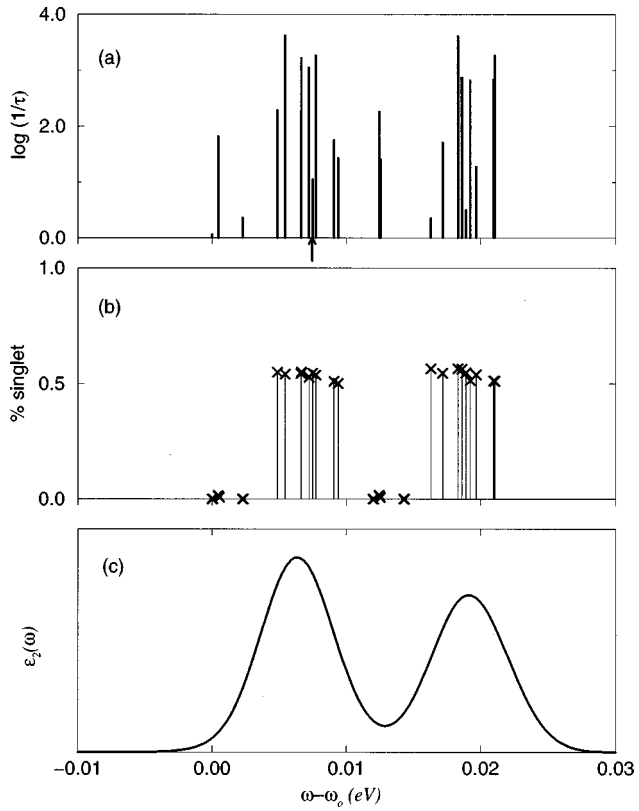

FIG. 8. Fine-structure calculation for the 1285-atom (18.3-Å radius) hydrogen-terminated Si nanocrystal. Symbols are the same as in Fig. 5. See Fig. 5 for definitions. $\omega_o = 1.374$ eV and $\eta = 0.0075$ eV for this nanocrystal.

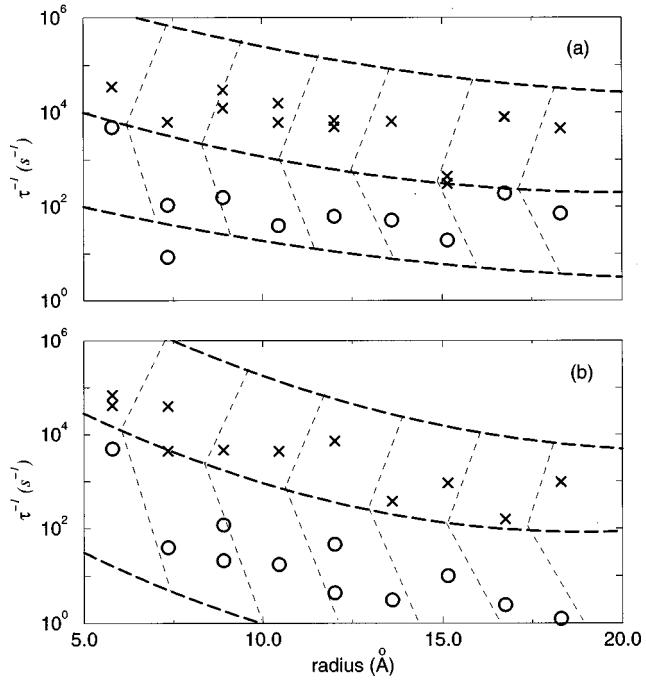

FIG. 9. Radiative decay rates (inverse lifetimes) of selected band-edge states, with the sp^3s^* tight-binding parameterization. (a) Hydrogen-terminated crystallites. (b) Surface-truncated crystallites. Crosses—bright band; circles—dark band. The demarcation of the bands, indicated by the dashed lines, is approximate, and states with lifetimes larger than one second are not shown.

perturbative features are successfully treated with this method, although it is not optimal for studying fine-structure effects. Using a restricted subspace diagonalization, we have then analyzed all the fine-structure effects, including Coulomb, exchange, and spin-orbit contributions. The current calculation differs from previous tight-binding studies in the incorporation of nearest-neighbor exchange contributions, and in distinguishing the screened the electron-hole Coulomb terms from the unscreened electron-hole exchange terms. The size dependence of the Coulomb and exchange interactions in silicon nanocrystals is shown to agree qualitatively with EMA estimates, although they differ in detail, especially at small sizes. Unlike EMA, the current results show that the exchange splitting scales as a^{-3} over a large size range. For nanocrystals of diameters up to ~ 36 Å, the spin-orbit effects are small compared to exchange splittings, and the singlet-triplet character profiles and radiative lifetimes computed in this work are qualitatively consistent with the two-state (triplet-singlet) model explanation of luminescence experiments in porous silicon. This indicates that nonspherical shapes may not be necessary for explaining the luminescence lifetimes in porous silicon, which consists of nanosize domains of up to ~ 31 Å in diameter.[49] Comparison with experiment shows that reasonable radiative lifetimes are obtained for the hydrogen-coated crystallites, although a quantitative computation would require that phonon-assisted pathways also be examined.[46] The improved agreement obtained relative to previous tight-binding results is assigned to the improved treatment of exchange here. Surface-truncated crystallites exhibit radiative lifetimes somewhat larger than their hydrogen-terminated counterparts. Other effects that may affect the optical properties of silicon nanocrystal excitons are phonon-induced Stokes shifts,[4,12] the possible existence of luminescent surface state,[50] and finite-size corrections to the dielectric function (which appear to be small for nanocrystal radius larger than 6 Å).[30]

ACKNOWLEDGMENTS

This work was supported by a grant from Sandia National Laboratories, Contract No. AR-9600, and by the Materials Design Initiative at Lawrence Berkeley National Laboratory, under ONR Contract No. N0001495F0099. K.B.W. thanks the A. von Humboldt Foundation for financial support. Computations were performed at the San Diego Supercomputer Center under an allocation of computer time on the C90 from the NSF Supercomputer Center.

APPENDIX: COULOMB AND EXCHANGE INTEGRALS AND SCREENING

The tight-binding calculation is cast in the $(sp^3)^4$-s^* basis. The Coulomb and exchange integrals in this local orbital basis, Eqs. (19) and (20), are $\langle sp_p^3 sp_q^3|(1/r)|sp_p^3 sp_q^3\rangle$ and $\langle sp_p^3 sp_q^3|(1/r)|sp_q^3 sp_p^3\rangle$, where p and q label the four hybridized orbitals. These matrix elements are most conveniently calculated in the $\{3s,3p_x,3p_y,3p_z,4s\}$ Cartesian basis, which we compute using the Slater-Koster orbital wave functions for silicon.[51] The interactions between hybridized orbitals are then expressed in terms of these Slater-derived

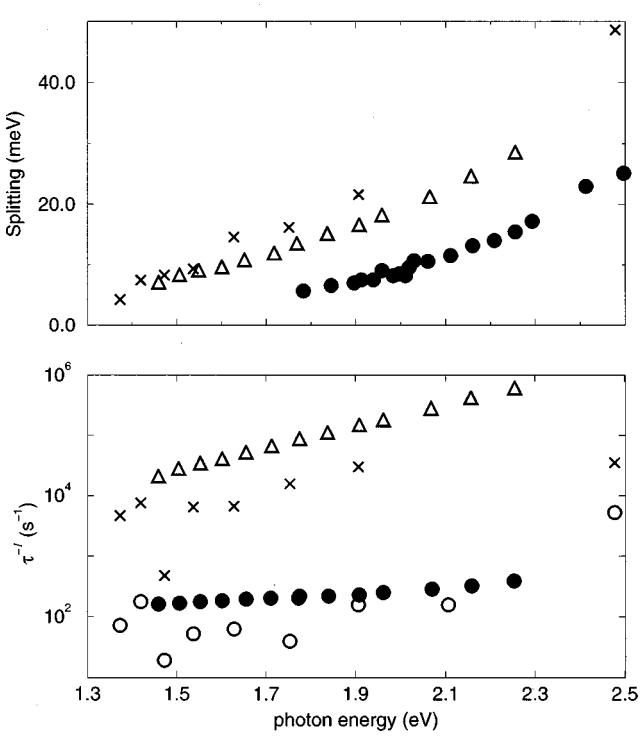

FIG. 10. Comparison of exchange splittings and radiative lifetimes derived from the tight-binding theory and from resonantly excited photoluminescence spectra (Ref. 8). (a) Exchange splitting. Crosses—theory (hydrogen-terminated crystallites); triangles—variable temperature τ measurement (see text); filled circles—onset measurement. (b) Radiative lifetimes. Crosses (theory) and triangles (Ref. 8)—bright band; circles (theory) and filled circles (Ref. 8)—dark band.

integrals, after discarding terms that involve more than two distinct atomic orbitals.

Coulomb and exchange matrix elements both contain a mixture of Coulomb and exchange integrals. Screening of the electron-hole interaction arises from polarization of the remaining electrons in the valence band by the electron-hole pair. Following Ref. 4, only the Coulomb matrix elements $\langle e'h'|\hat{H}_{\rm coul}|eh\rangle$ are screened; the exchange matrix elements $\langle e'h'|\hat{H}_{\rm ex}|eh\rangle$ are unrenormalized (Ref. 4; and see discussion below). Screening is accounted for here using a dielectric function $\epsilon(r)$ taken from Ref. 27. For integrals contributing to the exchange matrix element, $\langle e'h'|\hat{H}_{\rm ex}|eh\rangle$, $\epsilon(r)$ is then replaced by unity.

On-site Coulomb and exchange integrals are calculated directly if no screening is required. When screening is required, the on-site integrals can be evaluated by Fourier transforms. Thus, for example, Fourier transformation of

$$w_{\rm coul}(i3s,i3s)=\int dr_1 dr_2\,\frac{\rho_{3s}(r_1)\rho_{3s}(r_2)}{\epsilon(|r_1-r_2|)|r_1-r_2|} \quad \text{(A1)}$$

yields a one-dimensional integral in the reciprocal space. Since the precise magnitude of the on-site screening is not crucial to the results, for simplicity we therefore use the same approximation employed in Ref. 12, and scale all the screened on-site integrals by $w_{\rm coul}(i3s,i3s)/w^o_{\rm coul}(i3s,i3s)\approx 0.2$ in $\langle e'h'|\hat{H}_{\rm coul}|eh\rangle$, where $w^o_{\rm coul}(i3s,i3s)$ is the unscreened $3s$-$3s$ integral.

TABLE II. On-site Coulomb integrals (unscreened) in the sp^3s^* orbital basis, in units of eV. The four hybridized sp^3 orbitals are $|sp^3_a\rangle=\frac{1}{2}(|s\rangle+|p_x\rangle+|p_y\rangle+|p_z\rangle)$, $|sp^3_b\rangle=\frac{1}{2}(|s\rangle+|p_x\rangle-|p_y\rangle-|p_z\rangle)$, $|sp^3_c\rangle=\frac{1}{2}(|s\rangle-|p_x\rangle+|p_y\rangle-|p_z\rangle)$, and $|sp^3_d\rangle=\frac{1}{2}(|s\rangle-|p_x\rangle-|p_y\rangle+|p_z\rangle)$, respectively.

	sp^3_a	sp^3_b	sp^3_c	sp^3_d	s^*
sp^3_a	11.91	9.00	9.00	9.00	1.12
sp^3_b	9.00	11.91	9.00	9.00	1.12
sp^3_c	9.00	9.00	11.91	9.00	1.12
sp^3_d	9.00	9.00	9.00	11.91	1.12
s^*	1.12	1.12	1.12	1.12	0.95

Coulomb integrals which are centered on two different atoms are estimated using the Ohno formula[40,41]

$$w_{\rm coul}(i\gamma,i'\gamma') = \frac{1}{\epsilon(|r_i-r_j|)}\,\frac{14.397(\text{eV})}{\left[\left(\dfrac{14.397}{w^o_{\rm coul}(i\gamma,i\gamma')}\right)^2+(r_i-r_j)^2\right]^{1/2}}. \quad \text{(A2)}$$

Since the only orbital dependence here derives from the on-site term $w_{\rm coul}(i\gamma,i'\gamma')$ which is the same for all pairs of sp^3-hybridized orbitals, Eq. (A2) implies an orientation average over the two-centered integrals between sp^3-hybridized orbitals on different atoms. [Note that this description results in a distinction between off-site Coulomb terms involving sp^3 and s^* orbitals, which is absent in the simpler point charge approximation made in Ref. 12. Since in the sp^3s^* model the conduction states near the band edge have relatively large s^* character ($\sim 35\%s^*$) the resulting Coulomb energies are lower than would be obtained with a uniform (sp^3) value for the off-site Coulomb integrals. We note also that for a given dielectric function, the magnitude of the off-site Coulomb integrals resulting from Eq. (A2) is less than the value obtained with a point charge approximation (by 10–30%).] For unscreened exchange integrals centered on two different atoms, a multidimensional Fourier transform is applied to the product $\phi_{i\gamma}(r)\phi_{i'\gamma'}(r)$, and then the exchange integral is evaluated in Fourier space, in a manner similar to the calculation of on-site Coulomb integrals in Ref. 12. The largest contributions come from integrals that involve the s orbital and/or the p orbital along the bonding axis, and all other interactions are therefore neglected. When such exchange integrals occur in Coulomb matrix elements, screening is applied via the on-site rescaling factor alluded to above.

The resulting unscreened on-site Coulomb and exchange integrals in the sp^3s^* basis are listed in Tables II and Tables III, respectively, and the unscreened nearest-neighbor exchange integrals are listed in Table IV. The electron-hole Coulomb matrix elements $\langle e'h'|\hat{H}_{\rm coul}|eh\rangle$ are dominated by the on-site and off-site Coulomb integrals. Exchange contributions to the electron-hole Coulomb matrix elements are negligible in comparison. The electron-hole exchange matrix elements $\langle e'h'|\hat{H}_{\rm ex}|eh\rangle$ are dominated by the exchange contributions in Tables III and IV, and by some on-site Coulomb

TABLE III. On-site exchange integrals (unscreened) in the sp^3s^* orbitals basis, in units of eV. The four sp^3-hybridized orbitals have been defined in the captions of Table II.

	sp_a^3	sp_b^3	sp_c^3	sp_d^3	s^*
sp_a^3	11.91	0.73	0.73	0.73	0.00
sp_b^3	0.73	11.91	0.73	0.703	0.00
sp_c^3	0.73	0.73	11.91	0.73	0.00
sp_d^3	0.73	0.73	0.73	11.91	0.00
s^*	0.00	0.00	0.00	0.00	0.95

integrals. We note that the precise magnitudes of these integrals may depend on the orbital basis employed to evaluate them, here the Slater orbitals.

The issue of screening for the exchange interactions is actually quite complex. In the bulk, when expanded in Bloch functions, the exchange interactions can be subdivided into analytic and nonanalytic contributions, which correspond approximately to the short and long-range component respectively, of an expansion in Wannier functions.[52] The short-range (''analytic'') part of the exchange matrix elements should be unscreened[53] (see, however, Ref. 54). (A minor point here is that, strictly speaking, this requires that the ''electron'' and ''hole'' states be eigenstates of the single-particle Hamiltonian. The perturbative treatment of the spin-orbit coupling introduces an inconsistency here in principle, but as noted earlier the effect of the perturbation is weak enough that this may be neglected.) However, the ''nonanalytical'' portion, which includes the long-ranged term in Eq. (22) minus contributions from a ''core region,'' should actually be screened just like the Coulomb matrix elements.[52,55,56] In Ref. 4, a subset of the long-range nonanalytical exchange vanishes identically due to the symmetry of the spherical nanocrystals considered therein. We have found that, for large crystallites, screening the long-ranged terms in Eq. (22) modifies the bare exchange splitting by less than 10%. The correction is nonsystematic, varies in sign, and strongly depends on the size of the ''core'' region where screening is excluded. The splitting between the first bright and first dark states in the presence of spin-orbit coupling, depicted in Figs. 5–8, is less affected, and there is essentially no effect on the radiative lifetimes (Sec. III B). The effect of this screening on crystallites of less than 100 atoms is more significant. Since the effect of this long-range screening is small for the cluster sizes of concern here, we have left all contributions to the exchange matrix elements unscreened.

TABLE IV. Nearest-neighbor exchange integrals (unscreened) for the sp^3 orbitals in units of eV.

	Atom 1: bonding	Atom 1: nonbonding
atom 2: bonding	2.120	0.617
atom 2: nonbonding	0.617	0.174

Another issue for the exchange interaction is the contribution of the ''dipole''-like terms that arise from going beyond the pairwise overlap approximation in Eq. (22). Such dipole interactions allow the exciton to propagate in bulk crystals.[25] These terms contribute less than 0.5 meV for the small crystallites studied herein even when unscreened, and decreases with crystallite sizes.

[1] A. P. Alivisatos, Science **271**, 933 (1996); MRS Bull. **20**, 23 (1995).

[2] L. Brus, Appl. Phys. A **53**, 465 (1991); M. G. Bawendi, M. L. Steigerwald, and L. E. Brus, Annu. Rev. Phys. Chem. **41**, 477 (1990).

[3] L.-W. Wang and A. Zunger, Phys. Rev. Lett. **73**, 1039 (1994).

[4] T. Takagahara and K. Takeda, Phys. Rev. B **53**, R4205 (1996).

[5] J. C. Merle, M. Capizzi, P. Fiorini, and A. Frova, Phys. Rev. B **17**, 4821 (1978).

[6] G. Fishman, R. Romestain, and J. C. Vial, J. Phys. (France) IV **3**, 355 (1993); R. Romestain and G. Fishman, Phys. Rev. B **49**, 1774 (1994).

[7] P. D. J. Calcott, K. J. Nash, L. T. Canham, M. J. Kane, and D. Brumhead, J. Phys.: Condens. Matter **5**, L91 (1993).

[8] P. D. J. Calcott, K. J. Nash, L. T. Canham, M. J. Kane, and D. Brumhead, J. Lumin. **57**, 257 (1993).

[9] K. J. Nash, P. D. J. Calcott, L. T. Canham, M. J. Kane, and D. Brumhead, J. Lumin. **60&61**, 297 (1994).

[10] Acoustic phonons also contribute to the Stokes shifts. See, for example, Ref. 4.

[11] K. J. Nash, P. D. J. Calcott, L. T. Canham, and R. J. Needs, Phys. Rev. B **51**, 17 698 (1995).

[12] E. Martin, C. Delerue, G. Allan, and M. Lannoo, Phys. Rev. B **50**, 18 258 (1994).

[13] M. Nirmal *et al.*, Phys. Rev. Lett. **75**, 3728 (1995).

[14] A. I. Ekimov *et al.*, J. Opt. Soc. Am. B **10**, 100 (1993).

[15] N. A. Hill and K. B. Whaley, Phys. Rev. Lett. **75**, 1130 (1995).

[16] N. A. Hill and K. B. Whaley, J. Electron. Mater. **25**, 269 (1996).

[17] N. A. Hill and K. B. Whaley, Appl. Phys. Lett. **67**, 1125 (1996).

[18] P. Vogl, H. P. Hjalmarson, and J. D. Dow, J. Phys. Chem. Solids **44**, 365 (1983).

[19] A. Franceschetti and A. Zunger, Phys. Rev. Lett. **78**, 915 (1997).

[20] C. Delerue, M. Lannoo, and G. Allan Phys. Rev. Lett. **76**, 3038 (1996); N. A. Hill and K. B. Whaley, *ibid.* **76**, 3039 (1996).

[21] A. Zunger and L.-W. Wang, J. Phys. Chem. **98**, 2158 (1994).

[22] T. Takagahara, Phys. Rev. B **47**, 4569 (1993).

[23] N. A. Hill, and K. B. Whaley, Chem. Phys. **210**, 117 (1996).

[24] H. Haken, *Quantum Field Theory of Solids* (North-Holland, Amsterdam, 1976).

[25] R. S. Knox, *Solid State Physics* (Academic, New York, 1963), Vol. 5.

[26] F. Bassani and G. Pastori Parravicini, *Electronic States and Optical Transition in Solids* (Pergamon, Oxford, 1985).

[27] Z.-H. Levine and S. G. Louie, Phys. Rev. B **25**, 6310 (1982).

[28] The relation between the dielectric function, the screened Coulomb interaction, and the unscreened Coulomb interaction is discussed in, e.g., A. L. Fetter and J. D. Walecka, *Quantum Theory of Many-Particle Systems* (McGraw-Hill, San Francisco, 1971), Chaps. 3 and 4.

[29] N. A. Hill, Ph.D. thesis, University of California, Berkeley, 1996.

[30] K. Leung (unpublished).
[31] T. Nishino, M. Takeda, and Y. Hamakawa, Solid State Commun. **14**, 627 (1974).
[32] E. I. Blount, in *Solid State Physics* edited by F. Seitz and D. Turnball (Academic, New York, 1962), Vol. 13, p. 305.
[33] L. C. Lew Yan Voon and L. R. Ram-Mohan, Phys. Rev. B **47**, 15 500 (1993), and references therein.
[34] K. Leung, S. Pokrant, and K. B. Whaley (unpublished).
[35] V. I. Gavrilenko and F. Rebentrost, Surf. Sci. **331-333B**, 1355 (1995).
[36] D. E. Aspnes and A. A. Studna, Phys. Rev. B **27**, 985 (1983).
[37] See also R. Del Sole and R. Girlanda, Phys. Rev. B **48**, 11 789 (1993); A. Selloni, P. Marsella, and R. Del Sole, *ibid.* **33**, 8885 (1986).
[38] J. K. Cullum and R. A. Willoughby, *Lanczos Algorithms for Large Symmetric Eigenvalue Computations* (Birkhäuser, Boston, 1985), Vols. 1 and 2.
[39] The numerical packages `leval` and `levec` are available from the archive at `netlib@ornl.gov`. Degeneracies of the eigenstates are determined by repeating the diagonalization runs with different random seed numbers until no new states emerge.
[40] K. Ohno, Theor. Chim. Acta **2**, 219 (1964).
[41] K. Schulten, I. Ohmine, and M. Karplus, J. Chem. Phys. **64**, 4422 (1976).
[42] S.-Y. Lee and E. J. Heller, J. Chem. Phys. **71**, 4777 (1979).
[43] This approximation was also used in Refs. 15, 16, and 23.
[44] M. Suzuki, Prog. Theor. Phys. **56**, 1454 (1976).
[45] M. L. Mandich and K. D. Rinnen, Z. Phys. D **26**, 147 (1993).
[46] M. S. Hybertsen, Phys. Rev. Lett. **72**, 1514 (1994).
[47] D. L. Dexter, in *Solid State Physics*, edited by F. Seitz and D. Turnball (Academic, New York, 1958), Vol. 6, p. 353.
[48] Y. H. Xie, W. L. Wilson, F. M. Ross, J. A. Mucha, E. A. Fitzgerald, J. M. Macaulay, and T. D. Harris, J. Appl. Phys. **71**, 2403 (1992).
[49] S. Schuppler *et al.*, Phys. Rev. Lett. **72**, 2648 (1994).
[50] G. Allen, C. Delerue, and M. Lannoo, Phys. Rev. Lett. **76**, 2961 (1996).
[51] J. C. Slater, Phys. Rev. **36**, 57 (1930).
[52] U. Rossler and H.-R. Trebin, Phys. Rev. B **23**, 1961 (1981).
[53] L. J. Sham and T. M. Rice, Phys. Rev. **144**, 708 (1966).
[54] V. A. Kiselev and A. G. Zhilich, Fiz. Tverd. Tela (Leningrad) **15**, 2024 (1973) [Sov. Phys. Solid State **15**, 1351 (1975)].
[55] V. A. Kiselev and A. G. Zhilich, Fiz. Tverd. Tela (Leningrad) **14**, 1438 (1972) [Sov. Phys. Solid State **14**, 1233 (1974)].
[56] K. Ehara and K. Cho, J. Phys. Soc. Jpn. **51**, 3553 (1982).